

# Challenges and Optimization of Mu2e Proton Target Design with Radiative Cooling\*

Z. Liu<sup>†,1</sup>, J. Williams<sup>1</sup>, A. Makovec<sup>1</sup>, M. Hedges<sup>1</sup>, F. Pellemoine<sup>1</sup>, K. Yonehara<sup>1</sup>, G. Annala<sup>1</sup>, K. Lynch<sup>1</sup>, M. Bloomer<sup>2</sup>, J. Popp<sup>3</sup>, A. Edmonds<sup>3</sup>, J. Miller<sup>4</sup>

<sup>1</sup>Fermi National Accelerator Laboratory, Batavia IL, USA

<sup>2</sup>York College / CUNY, Jamaica NY, USA

<sup>3</sup>Emory University, Atlanta GA, USA

<sup>4</sup>Boston University, Boston MA, USA

## Abstract

Mu2e, the Muon-to-Electron Conversion Experiment, aims to identify physics beyond the Standard Model, namely, the conversion of muons to electrons without the emission of neutrinos. The muons are produced from pions generated in a production target when it is hit by an 8 GeV proton beam from the Fermilab Booster/Main Injector. The proton target design space is strongly constrained by a one-year operating lifetime and the need for radiative cooling in a vacuum environment. Uncertainties in the lifetime of the existing baseline design – a monolithic, segmented tungsten target – are large, particularly due to unknown impacts of radiation damage at the very high proton fluences expected in the experiment. We have begun evaluation of a new design utilizing Inconel 718 over the WL10 used in the existing target design. As a result, the structural design of the target has evolved significantly. This evolution focuses on lowering the target temperature, minimizing obstruction to muons, increasing structural stability, maximizing fatigue lifetime, simplifying the fabrication process, and more. The thermal management, structural stability and fatigue lifetime are emphasized here. These optimizations have led to a promising new target design for the Mu2e experiment.

## INTRODUCTION

The Muon-to-Electron Conversion Experiment, Mu2e in Fermilab, is designed to observe a specific theoretical process, the conversion of muons to electrons without the emission of neutrinos [1]. It begins with an 8 GeV proton beam from Fermilab Booster/Main Injector to produce muons and aims to provide evidence of new physics. As shown in Fig. 1, the proton beam enters the Production Solenoid and hits the Production Target, which generates pions. Then, muons are produced via pion decay. These muons are directed through the Transport Solenoid and stopped in the Detector Solenoid by the Muon Stopping Target where the muon to electron conversion occurs. The Detector Solenoid also houses the Tracker and Calorimeter required to identify and analyse conversion electrons from the stopping target.

The production target design is fundamental to the success of Mu2e experiment since it is where to get the muons at the first place. The size and shape of the production target, the target supports and the clearance inside the Production Solenoid have all been designed to maximize the yield of stopped muons [2]. The production target design of

Hayman, top-left in Fig. 2, is made from tungsten, a high Z material, to maximize pion production while the geometry is designed to minimize pion reabsorption. The Hayman target is 220 mm long with its core of 6 mm in diameter and four fins to increase surface for radiation cooling. At right in Fig. 2, the target support of bicycle mount structure, a small physical profile of six spokes holding the target to the bicycle ring, is designed to minimize scattering and absorption of pions and muons and allow pions and muons to pass through within the acceptance of the Transport Solenoid. The whole assembly of the bicycle ring and the target shall be removed through a remote handling system (RHS). A one-year operating lifetime is expected for the production target, which triggers further investigation of the challenge due to radiation damage and optimization thereafter.

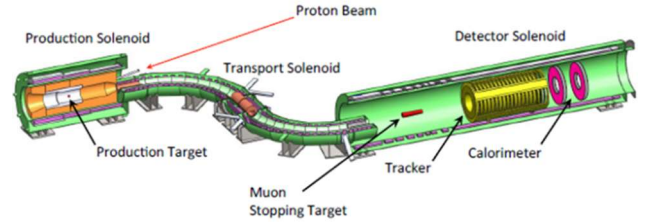


Figure 1: Schematic of Mu2e Experimental Setup.



Figure 2: Mu2e production targets and bicycle wheel mount structure (right) [2].

Radiation damage to the production target is a key factor in maintaining its performance during its serve time. Radiation damage may change mechanical properties of the material, including mechanical strength and thermal conductivity. The degree of radiation damage is often quantified with displacements per atom (DPA) at lattice level. As DPA increases, the material's ability to manage heat and absorb shock decreases, accelerating degradation and failure. Unfortunately, recent application of tungsten in highly

irradiated conditions has shown that it's possible harmfully susceptible to radiation damage [3]. DPA can be calculated per incident proton interacting with the target material by using simulation tools like FLUKA [4, 5]. For a tungsten target subjected to an unprecedented 8 GeV proton beam in Mu2e experiment, simulation substantiates that an extraordinary amount of radiation damage would likely occur causing stability issue [6].

A pion and muon production study from the International Muon Collider Collaboration (IMCC) shows that tungsten is the optimal material choice for a muon production target for the highest yield, while for some lower density materials like nickel and molybdenum may have similar muon yield [7]. With the same target geometry and Mu2e beam conditions, G4Beamline [8] simulation of muon production per proton on target (POT) shows that the muon production does not increase linearly with target density [9]. Nickel-based Inconel is a contender for the first Mu2e target material [10].

Inconel 600 was used in the Fermilab Antiproton Source [11], but there is not any report of post irradiation examination (PIE) on this target. Recently a solution-annealed Inconel 718 proton beam window at the Spallation Neutron Source was reported with observation of an increase in ductility, rather than embrittlement, under 10 DPA of proton irradiation [12]. Preliminary physics analysis estimates a peak of 10 dpa after proton irradiation for Inconel 718 target in one-year of Mu2e running. In addition, Inconel 718 has high emissivity, up to 0.9 of hemispherical total emissivity [13], which suits radiation cooling as a restriction for the design. These motivate the design of the Stickman target as shown in left bottom in Fig. 2.

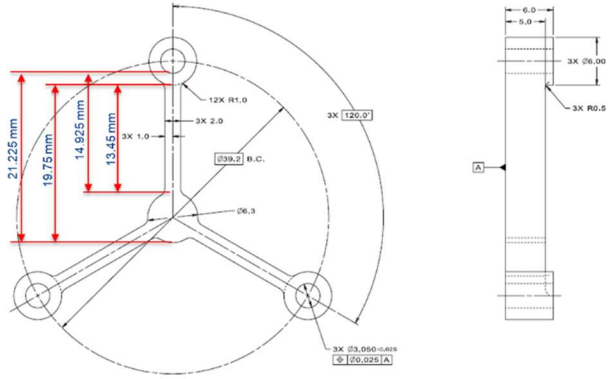


Figure 3: Stickman target plate (typical).

The new target shall fit within the confines of the RHS for safely remove and replacement of the target. To serve that purpose, the bicycle wheel mount structure in Fig. 2 stays the same except minor changes such as Inconel 718 for the spokes for the new target design. The new target, Stickman, has three fins rather than four fins, which is easier to deal with for assembly and mount. The Stickman target is of an assembly of thirty-five identical pieces of plates (Fig. 3), three bars, two end rings, and six spacers. It's expected to simplify the fabrication process and isolate failure of a single plate from affecting the rest when the target is fabricated by pieces. The overall length and core

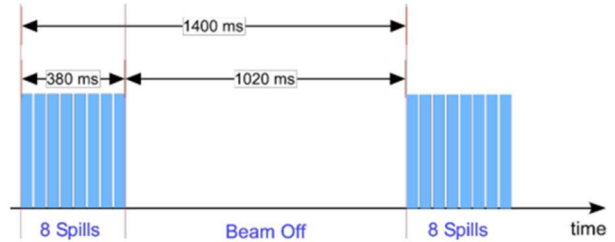
diameter of the Stickman target stay the same as the Hayman design.

This significant evolution of the target design focuses on lowering the target temperature, minimizing obstruction to muons, increasing structural stability, maximizing fatigue lifetime, simplifying the fabrication process, and more. Those ongoing activities, such as simplifying fabrication process and evaluation of Inconel mechanical properties change from proton beam bombard, are not covered here. The thermal management, structural stability and fatigue lifetime are emphasized here. These optimizations have led to a promising new target design for the Mu2e experiment.

## THERMAL MANAGEMENT

### Proton Beam for Mu2e

Macro-structure of the beam on the Mu2e proton target is illustrated in Fig. 4. Two Booster proton batches, each containing four spills or  $4.0 \times 10^{12}$  protons with a kinetic energy of 8 GeV, are extracted and designated for Mu2e. For each spill, the proton target will see a train of proton pulses lasting 43.1 msec followed by a 5 msec reset period with no beam. This is repeated eight times during each Main Injector cycle for a total beam on time of 380 msec. At the end of the eight spills, beam to Mu2e is off for 1020 msec. The maximum number of protons per spill is  $1.25 \times 10^{12}$ , which is counted for thermal management as a conservative approach. The power per spill of the protons is about 1602 J within 43.1 msec.



### Energy Deposition in Stickman Target

When the protons hit the target, part of the energy is deposited in the material through interaction. The energy deposition (Edep) is calculated with FLUKA. The mesh size for the Edep calculation is generally 0.033 cm along beam direction, Z-axis, and 0.015 cm along the other orthogonal directions, X- and Y- axes for most components of the target assembly. The exception goes to the bicycle ring with mesh size of 0.125 cm along all X, Y, and Z directions, and to the spokes with mesh size of 0.025 cm along X and Y directions and 0.050 cm along Z direction. When these Edep data are imported into the commercial software ANSYS for finite element analysis (FEA), the FEA mesh size is 0.5 mm or smaller. To map the import data to the FEA meshing, ANSYS takes profile fit to obtain the value at corresponding nodes. This explains the discrepancy of the peak value of the Edep between FEA and the excel as import format in Fig. 5. The total Edep values from FEA and the excel agree on each plate. The sequential number in Fig. 5 represents the target plates along beam direction or

Z-axis. This comparison serves as a sanity check for the input.

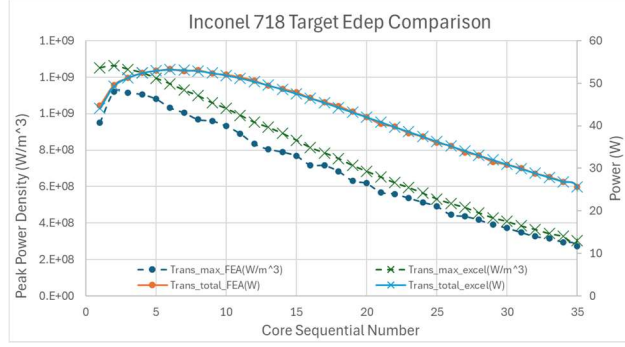


Figure 5: Energy deposition in Stickman target plates.

### Thermal Analysis

The heat that is deposited in the target will dissipate through the radiation, which follows the Stefan-Boltzmann Law with the governing principle of Eq. (1).

$$P = \sigma \times \varepsilon \times A \times (T^4 - T_b^4) \quad (1)$$

where,  $P$  is the energy deposition in the Target from interaction with the Protons,  $\sigma$  Stefan-Boltzmann constant,  $\varepsilon$  surface emissivity,  $A$  the radiation surface,  $T$  temperature of the target, and  $T_b$  temperature of the surroundings.

Calculation following Eq. (1) may be performed for a rod of radius of 22.6 mm resembling the radiation surface of the target of thirty-five plates (Fig. 3). With the power of about 400 W (Fig. 5), the hemispherical total emissivity 0.85 at 600 °C (Fig. 6), and surrounding temperature 25 °C, the average target temperature is about 530 °C.

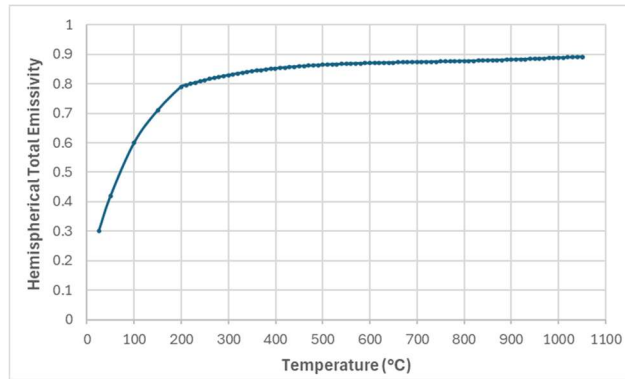


Figure 6: Hemispherical total emissivity of Inconel 718 oxidized at 1000 °C, with assumption of emissivity 0.3 at room temperature and curve fitting between 25 °C and data above 200 °C [13].

The temperature distribution within the target assembly is revealed through FEA. Temperature dependent material properties [14, 15, 16, 17] are applied in the FEA, while Table 1 lists as references the corresponding properties at room temperature and at 648.9 °C / 1200 °F. After 14 s cycling from temperature distribution of steady-state FEA, as shown in Fig. 7, the peak temperature cycles with the proton beams on and off, indicating the status of stable in terms of thermal balance. For a single cycle of heating in Fig. 8, peak temperature occurs in the target plate and low temperature 62 °C in the bicycle ring. On the right side is

an enlarged sectional view of the 6th target plate showing distribution of temperature ranging from the maximum value 656.17 °C to 432.05 °C.

Table 1: Inconel 718 Properties (AMS 5596 sheet/plate, AMS 5662 and 5663 bars and rings) [14-17]

Properties	At 21 °C	At 649 °C
Density	8.19 g/cc	8.00 g/cc
Young's Modulus (E)	200 GPa	164 GPa
Torsional Modulus (G)	77.2 GPa	62.7 GPa
Poisson's Ratio (ν)	0.294	0.283
Tensile Strength	1241 MPa	965 MPa
Yield Strength	1034 MPa	793 MPa
Thermal Conductivity	11.4 W/m-K	21.2 W/m-K
CTE (α)	12.3 μm/m-°C	14.98 μm/m-°C
Specific heat $C_p$	428 J/kg-K	595 J/kg-K

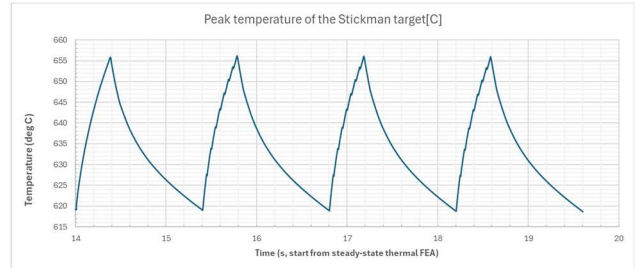


Figure 7: Peak temperature cycles with the heating and cooling. After 14 s cycling from temperature distribution of steady-state FEA, the first cycle at left is for heating evenly distributed within 380 ms, while the other three cycles for eight times of 43.1 ms beam-on and 5 ms beam-off and followed by 1.02 s beam-off.

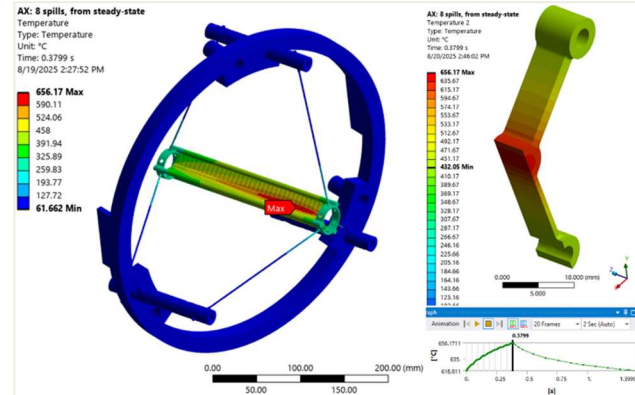


Figure 8: Temperature distribution of the target assembly

## STRUCTURAL ANALYSIS

### Stress Analysis

For an isotropic elastic material, Eq. (2) governs the stress-strain relationship within the solid [18]. The first two terms at right hand side calculate stresses from structural rather than thermal strains. The last term shows when  $T$  is greater than  $T_0$  the constraints exert a compressive force on the material. A tensile force occurs when  $T$  is less than  $T_0$ . Without constraints the thermal expansion or contraction leads to zero stresses. The zero stresses in the fins of the target plate (left image in **Error! Reference source not found.**) demonstrate no constraint is applied, while non-



zero stresses in the core and corner are subject to geometrical constraints to the thermal expansion. In comparison the target plate has constraint from the support of three rods that are fixed at end faces (right image in **Error! Reference source not found.**), which results in non-zero stresses in the fins. The maximum value of von-Mises stress increases from 98.8 MPa to 118.8 MPa when the support is applied. At 650 °C the Inconel 718 yields at 793 MPa (**Error! Reference source not found.**), which tells that the safety factor of the target plate is about 6.6 without counting radiation damage.

$$s_{ij} = \frac{E\theta}{(1+\nu)(1-2\nu)}(e_{11} + e_{22} + e_{33})\delta_{ij} + 2Ge_{ij} + \frac{E\alpha}{1-2\nu}(T - T_0)\delta_{ij} \quad (2)$$

The peak temperature and maximum thermal stress due to heating from the first 8 spills of the proton beam are 92 °C and 75 MPa, as shown in Figure 1. The stress comes from geometrical constraint to thermal expansion. It's further lower.

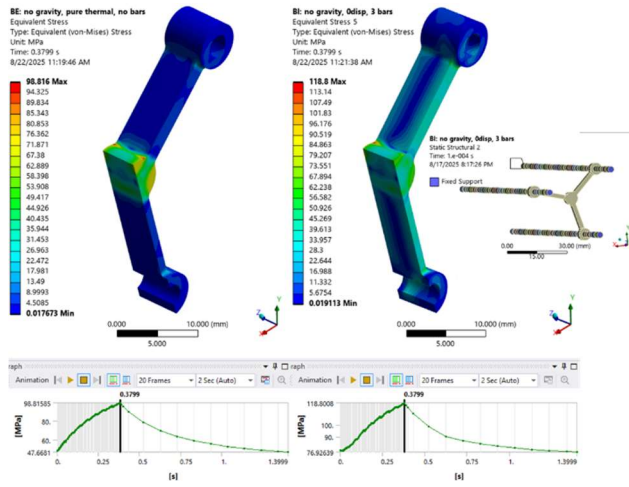


Figure 9: Stress of the target plate #6. Left: thermal stress without constraints. Right: thermal stress with fixed surfaces of three rods and frictionless contacts.

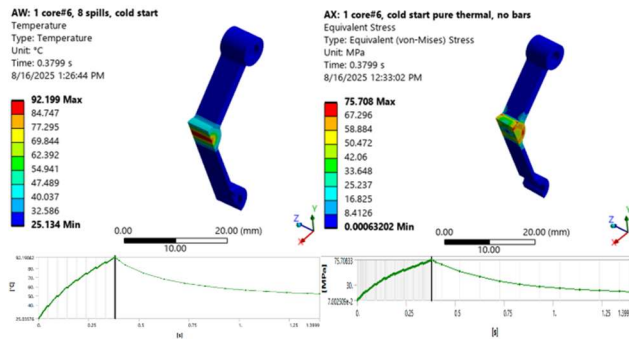


Figure 1: Temperature and thermal stress of Stickman target subjected to bombard of the first 8 spills of proton beam

### Fatigue, Rupture Life, Creep Rate, and Vibration Analysis

The peak stress rises to 118.8 MPa and goes down to 76.9 MPa in one cycle of beams on and off, as shown on Fig. 9. With 1.4 s as the period of one cycle, the one-year

operational lifetime for the target means  $2.25 \times 10^7$  cycles per year. The cycle number and stress are much less than  $10^8$  cycle under stress 582 MPa in Table 2 for the concern of fatigue. Similarly with the stress level, rupture life and creep rate are beyond concern as well if these properties won't be decreased by half by radiation damage to the material.

Table 2: Fatigue, rupture life and creep rate of Inconel 718 at 649 °C [14]

Temperature	Fatigue		Rupture		Creep Rate	
	Cycle	Strength	Rupture life	Stress	Creep rate	Stress
649 °C	$10^8$	582 MPa	800 hr	485 MPa	0.000002	485 MPa

Although thermal stress in the Inconel target plate is not high, it might be amplified through oscillation in harmony. The modal analysis through FEA reveals that the mode shape of expansion oscillates at 298087 Hz, as shown in Figure 2. It indicates that neither the stress wave nor the thermal wave in this target plate should bounce back and forth at this frequency.

The speed of sound in solids,  $u_s$ , may be estimated with Eq. (3) [18], while the speed of thermal wave  $u_T$  with Eq. (4) [19].

$$u_s = \sqrt{E/\rho} \quad (3)$$

$$u_T = \sqrt{K/(\rho C_p \tau)} \quad (4)$$

where Young's modulus E, density  $\rho$ , thermal conductivity K, and specific heat  $C_p$  are listed in Table 1, while  $\tau$  is the relaxation time or build-up time for the onset of the thermal flux after a temperature gradient is suddenly imposed on the sample. The value of  $\tau$  is at the order of  $10^{-12}$  s for most materials at room temperature. The sound velocity 5820 m/s and thermal waves 1694 m/s in room temperature in Inconel 718 are and, correspondingly. The frequency for sound and thermal waves in Inconel 718 are listed in Table 3. The frequency 294684 Hz for distance 19.75 mm (**Error! Reference source not found.**) is close to 298087 Hz. The reflection rate of the stress wave from either of the curved surfaces is low, and the mismatch of the cross area between the core and fins shall further damp the wave propagation. Stress oscillation is not a concern as well.

AY: Single core, Inconel718  
Total Deformation  
Type: Total Deformation  
Frequency: 298087.1 Hz  
Unit: m  
3/19/2025 4:48 PM

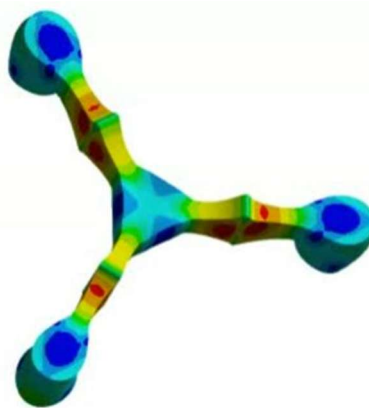
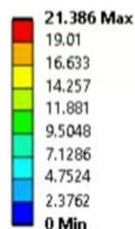


Figure 2: Mode shape and frequency of expansion.

Table 3: Wave propagation in Inconel 718 target.

Distance	Sound velocity (5820 m/s)	Thermal wave velocity (1694m/s)
13.45 mm	432714 Hz	125948 Hz
14.925 mm	389950 Hz	113501 Hz
19.75 mm	294684 Hz	85772 Hz
21.225 mm	274205 Hz	79812 Hz

## SUMMARY

Radiation damage to target material has been a major concern for Mu2e production target design. The observation of an increase in ductility, rather than embrittlement, of a solution-annealed Inconel 718 proton beam window under 10 DPA of proton irradiation leads to a new design of Mu2e target of Inconel 718. While the radiation tests for material properties of Inconel 718 are ongoing, thermal and structural analyses of the optimized target design predict its performance. The maximum temperature is about 656 °C, above which the strength of Inconel 718 descends dramatically [14]. The maximum stress is at the level of 120 MPa, which leads to a safety factor of 6.6 with respect to its yield point. This stress level also predicts that the target may perform well within one-year operational lifetime, including more than one year of fatigue lifetime and rupture life with zero creep, unless these material properties are decreased by more than half due to radiation damage. It's known that annealing and aging play important roles in material properties, which have been considered in design and fabrication. This prediction shows that these optimizations lead to a promising new target design for Mu2e experiment.

## REFERENCES

- [1] L. Bartoszek, et al., “Mu2e Technical Design Report”, physics.ins-det, 2015. <https://arxiv.org/abs/1501.05241v2>
- [2] C. N. Steffel, “Target Practice: Perfecting the Mu2e Production Target”, <https://news.fnal.gov/2019/11/target-practice-perfecting-the-mu2e-production-target>
- [3] J. Habainy, et al, “Mechanical properties of tungsten irradiated with high-energy protons and spallation neutrons”, J. Nucl. Mater. Vol. 514, pp. 189-195, 2019. <https://doi.org/10.1016/j.jnucmat.2018.12.003>
- [4] C. Ahdida, et al., “New Capabilities of the FLUKA Multi-Purpose Code”, Front. Phys. Vol. 9, Article 788253, 2022. <https://doi.org/10.3389/fphy.2021.788253>
- [5] G. Battistoni, et al., “Overview of the FLUKA code”, Annals of Nuclear Energy, vol. 82, pp. 10-18, 2015. <https://doi.org/10.1016/j.anucene.2014.11.007>
- [6] M. Hedges and M. Bloomer, "High-Power Targetry for Muon Production", physics.acc-ph, 2025, <https://doi.org/10.48550/arXiv.2501.10556>
- [7] C. Densham, “Prospects and Considerations for a Fluidized Tungsten Target for the Muon Collider”, [https://indico.cern.ch/event/1250075/contributions/5348859/attachments/2670245/4628813/IMCC\\_fluidized-tungsten-target\\_v1.pdf](https://indico.cern.ch/event/1250075/contributions/5348859/attachments/2670245/4628813/IMCC_fluidized-tungsten-target_v1.pdf)
- [8] T. J. Roberts, et al., “G4Beamline Particle Tracking in Matter-dominated Beam Lines”, Conf. Proc. C 0806233, WEPP120, 2008.
- [9] M. Bloomer, “Analysis of Potential Target Materials for the Mu2e Production Target”, Aug. 2024, <https://doi.org/10.2172/2426573>
- [10] M. Bloomer, “Analysis of Potential Target Materials for Production of High Intensity Secondary Beams”, thesis, Emory University, 2025. <https://etd.library.emory.edu/concern/etds/44558f914?locale=de>
- [11] J. Morgan, “Pbar Production Target Performance in Run II”, Apr. 2003. <https://doi.org/10.2172/1985137>
- [12] D. A. McClintock, et al., “Observations of radiation-enhanced ductility in irradiated Inconel 718: Tensile properties, deformation behavior, and microstructure”, Acta Mater. vol. 231, article 117889, 2022. <https://doi.org/10.1016/j.actamat.2022.117889>
- [13] G.A. Green, et al., “Total hemispherical emissivity of oxidized Inconel 718 in the temperature range 300-1000 °C”, Exp. Therm. Fluid Sci., vol. 22, No. 3-4, pp.145-153 ,2000. [https://doi.org/10.1016/S0894-1777\(00\)00021-2](https://doi.org/10.1016/S0894-1777(00)00021-2)
- [14] Data sheet, SMC-045, Special Metals Corporation, Huntington, WV, Sept 2007. <https://www.specialmetals.com/documents/technical-bulletins/inconel/inconel-alloy-718.pdf>
- [15] M. Fukuhara and A. Sanpei, “Elastic moduli and internal frictions of Inconel 718 and Ti-6Al-4V as a function of temperature”, J. Mater. Sci. Lett., vol.12, p1122-1124, 1993. <https://doi.org/10.1007/BF00420541>
- [16] US Air Force, “Metallic Materials and Elements for Aerospace Vehicle Structures”, MIL-HDBK-5H, pp.6-51, 1 Dec 1998. <https://archive.org/details/milhdbk-5-h>
- [17] S.H. Lee, et al., “Effect of Heat Treatment on the Specific Heat Capacity of Nickel-Based Alloys”, Int. J. Thermophys,

vol. 27, pp.282-292, 2006. <https://doi.org/10.1007/s10765-006-0029-2>

- [18] Y.C. Fung and P. Tong, "Classical and Computational Solid Mechanics", World Scientific Publishing Co. Pte. Ltd, 2001
- [19] E. Marin et al., "On thermal waves' velocity: some open questions in thermal waves' physics", Rev. mex. fis. E, vol.62, pp.1-4, 2016.